PHYSICS OF FLUIDS VOLUME 11, NUMBER 11 NOVEMBER 1999

Vortex interaction and mixing in a driven gaseous axisymmetric jet

T. R. Meyer, J. C. Dutton, and R. P. Lucht
Department of Mechanical and Industrial Engineering, University of Illinois at Urbana–Champaign, Urbana, Illinois 61801

(Received 29 September 1998; accepted 22 July 1999)

Vortex formation and merging are investigated in the near field of a driven axisymmetric jet. Acoustic forcing is used to obtain repeatable vortex pairing events, and simultaneous passive scalar and cold-chemistry planar laser-induced flourescence are used to obtain instantaneous images of molecularly mixed jet fluid fraction. The time-varying scalar dissipation field and area-averaged stirredness of the vortex core region are measured at various stages of vortex interaction. These mixing properties are analyzed in conjunction with the observed vortex dynamics, such as the time-dependent vortex convection velocity. The results indicate that there are several phases of the pairing event with distinct mixing characteristics, including vortex roll-up, interaction, coalescence, and reentrainment. Vortex roll-up is nearly laminar with molecular diffusion between the layers of jet and co-flow fluid. The most dramatic change in the mixing state of the leading vortex, which includes the appearance of a uniformly mixed core region, occurs as the trailing vortex approaches and interferes with co-flow fluid entrainment. Vortex coalescence is marked by gross deformation and stretching of the trailing vortex, and rapid homogenization of the diffusion layers. Finally, re-entrainment of pure fluid after the pairing event results in an elongated, nonrotating structure. These stages of vortex pairing correspond to the temporal evolution of vorticity observed in previous studies. © *1999 American Institute of Physics.* [S1070-6631(99)01711-0]

I. INTRODUCTION

Previous studies of axisymmetric jets have shown that large-scale vortical structures dominate the entrainment of free-stream fluid into the shear layer,[1,2] and indicate that the mean concentration profile is an inadequate descriptor of mixing in the near field and self-similar regions.[3] The ability to obtain instantaneous, quantitative measurements of concentration with various laser diagnostic techniques has allowed the use of probability density functions to characterize the mixing state of large-scale turbulence in liquid[4,5] as well as gaseous[6,7] shear layers. The detailed vortex dynamics, however, are not obvious from these statistical results. More direct visualizations of vortex behavior in gaseous jets are made possible by high-speed imaging techniques,[8,9] although well resolved, time-correlated measurements of the internal vortex layers have been obtained only in liquid shear layers.[10,11] The results of the latter studies are limited to non-interacting vortices, and it is unclear how their results apply to gaseous shear layers due to the large difference in the Schmidt number for liquids and gases.[4,12]

As an alternative to using high-speed imaging techniques, external forcing can provide a deterministic flow field for high-resolution, time-correlated studies of vortex structure in gaseous shear layers. Hussain and Zaman[13] report the use of controlled excitation in an axisymmetric jet, for example, to obtain vortex structures with streamline patterns, aspect ratios, and spacings that are similar to naturally occurring structures. By probing the jet at different phases with respect to the excitation pulse, the evolution of vortical structures can be studied using very small time increments without the trade-off of reduced spatial resolution. This is especially useful in gaseous flows for which turbulent time scales are an order of magnitude smaller than for liquids.

One disadvantage of the driven axisymmetric jet is that the repeatability and two dimensionality of vortical structures is only ensured in the near field adjacent to the jet exit where random disturbances are minimal. Nevertheless, the jet near field is of fundamental interest in combustion applications where vortical structures have a large impact on the structure and stabilization of jet flames.[14,15] Vortex pairing in the near field plays a significant role in the transition to the self-similar, turbulent regime.[16] Thus, it is also of interest from a modeling perspective to study vortex dynamics in the near field. In recent years, significant progress has been made using direct numerical simulations (DNS) and large eddy simulations (LES) for modeling flows with vortex merging and vortex–flame interactions.[17–19] The driven, isothermal jet provides a deterministic flow field that can be used to obtain quantitative measurements of vortex formation and interaction for the validation of such models.

Perhaps the most detailed study of vortex pairing in a driven jet was performed by Zaman and Hussain,[13,20] who used hot-wire measurements to track the evolution of vorticity, Reynolds stress, and local velocity during four phases of the pairing event. They also compared their findings, at least qualitatively, with smoke-streak visualizations. More recently, Leboeuf and Mehta[21] used acoustic forcing in a planar shear layer to study the evolution of vorticity in a spanwise roller pairing. These studies have provided valuable information on vortex dynamics via measurements of the velocity field during vortex interactions. The current investigation differs in that it is primarily concerned with the evolution of the mixing state within the large-scale structures.

Paul *et al.*[22] measured the concentration field in a driven axisymmetric jet using passive scalar planar laser-induced fluorescence (PLIF), and Grinstein *et al.*[15] studied the near field of a round jet under combined axial and azimuthal excitation using OH PLIF. Schauer[14] and Hancock[23] studied the driven vortex–flame interaction in an axisymmetric jet using particle image velocimetry, coherent anti-stokes Raman spectroscopy (CARS) temperature measurements, reactive Mie scattering, nitric oxide (NO) LIF, and OH PLIF imaging. Other researchers have studied the effects of forcing frequency on vortex behavior,[24,25] or to predict the transition to small-scale turbulence.[16] These studies typically do not consider the effects of streamwise vortex merging on the time-dependent state of molecular mixing within the shear layer.

The goal of the current investigation is to use a dual-tracer PLIF technique to study time-correlated vortex formation, pairing, and mixing in a gaseous axisymmetric jet. This is accomplished by using a low-amplitude acoustic pulse to create a repeatable, pseudolaminar vortex mixing event. The time-dependent vortex convection velocity, molecularly mixed jet fluid fraction, viscous core diameter, and scalar dissipation will be used to identify distinct stages of vortex evolution and pairing.

II. MIXING THEORY

According to the Broadwell–Breidenthal–Mungal[12,26] model, the turbulent mixing process begins with the entrainment of pure fluid into the mixing layer and follows a cascade of scales to the Kolmogorov microscale. At this point, the small mixing lengths and large interfacial areas result in almost instantaneous molecular mixing. Structures within the flow field consist of either pure fluid, strained laminar diffusion layers, or a homogeneous mixture. Deviations from this idealized model have been observed at high Reynolds numbers ($\mathrm{Re}_\delta > 30\,000$).[5–7] However, the model describes the structure of the shear layer quite accurately for intermediate Reynolds numbers ($\mathrm{Re}_\delta < 30\,000$),[5,27] as should be the case for the driven axisymmetric jet of the current investigation. Thus, we expect to see inviscid vortex rollers with laminar diffusion layers, possibly with homogeneous cores where pseudoturbulent random behavior has been detected in previous experiments.[16]

Assuming from universal equilibrium theory[28,29] that viscous dissipation takes place in the high wave-number range of the kinetic energy spectrum, then dimensional analysis indicates that the dissipative (Kolmogorov) length scale is[30]

$$\lambda_K = \left(\frac{\nu^3}{\epsilon}\right)^{1/4} \propto \delta\, \mathrm{Re}_\delta^{-3/4}, \tag{1}$$

where ν is the kinematic viscosity, ϵ is the kinetic energy dissipation rate per unit mass, δ is the local shear layer width, and Re_δ is the outer scale Reynolds number based on the velocity difference and shear layer width. The Batchelor scale, $\lambda_\mathrm{B} = \lambda_K\, \mathrm{Sc}^{-1/2}$, accounts for Schmidt number effects,[31] although $\lambda_\mathrm{B} = \lambda_K$ for gases in which $\mathrm{Sc} \approx 1$. The smallest mixing length scale (strain-limited diffusion), λ_D, is presumed to be proportional to the Batchelor scale:[31]

$$\lambda_D = \Lambda \lambda_\mathrm{B} = \Lambda\, \delta\, \mathrm{Re}_\delta^{-3/4}\, \mathrm{Sc}^{-1/2}, \tag{2}$$

where the proportionality constant was measured by Buch and Dahm[32] in a gaseous round turbulent jet to range from $\Lambda = 5.6$ to 16.8, with a mean value of $\Lambda = 11.2$. Su and Clemens[33] calculated a value of $\Lambda = 13.8$ in a gaseous planar turbulent jet, while Dowling and Dimotakis[34] estimated a value of $\Lambda = 25$ from the high wave-number drop-off in the scalar spectrum of a gaseous round turbulent jet. The calculation of λ_D from the integral scale provides a means of estimating whether a given experimental technique has sufficient spatial resolution for accurate measurements of the scalar dissipation field:

$$\text{scalar dissipation} = \nabla C \cdot \nabla C, \tag{3}$$

where C is the concentration of jet fluid in gmol/m^3 for the current investigation. The scalar dissipation is the rate at which nonuniformities are reduced by molecular diffusion, and can therefore be interpreted as a measure of the instantaneous rate of molecular mixing.[11,31,32]

Another quantity that is used to describe the mixing state is referred to as the mixedness. For regions where the average mixture fraction of each fluid is 0.5, mixedness is defined by Cetegen and Mohamad[10] as

$$\xi_\mathrm{mix} = \frac{4}{A}\int_A \xi(1-\xi)\,dA, \tag{4}$$

where ξ is the fraction of fluid from one of the fluid streams and A is the area of a given region. When a fluid element within the given region is at $\xi = 0$ or 1, it contains pure fluid from one of the streams and there is no contribution to the ξ_mix integral. The maximum value of mixedness occurs when $\xi = 0.5$ everywhere, in which case $\xi(1-\xi) = 0.25$ and $\xi_\mathrm{mix} = 1$. When the average mixture fraction is not 0.5, however, a more general expression is required:[35]

$$\xi_\mathrm{mix} = \begin{cases} \dfrac{1}{A}\displaystyle\int_A \frac{\xi}{\xi_A}\left(2 - \frac{\xi}{\xi_A}\right) dA & \text{for } \xi \leqslant \xi_A \\[2ex] \dfrac{1}{A}\displaystyle\int_A \frac{-\xi^2 + 2\xi\xi_A + 1 - 2\xi_A}{(1-\xi_A)^2}\, dA & \text{for } \xi > \xi_A \end{cases}, \tag{5}$$

where ξ_A is the average mixture fraction for one of the fluids in the given region. With this formulation, ξ_mix is properly normalized to vary from zero to unity. Unlike Eq. (4), however, Eq. (5) is weighted such that if $\xi_A = 0.8$, for example, values of $\xi = 0.7$ contribute to the ξ_mix integral more than values of $\xi = 0.5$. While ξ_mix is often referred to as the mixedness, the finite resolution of flow imaging equipment (above the Batchelor scale) means that ξ_mix does not necessarily measure the state of *molecular* mixing, since the fluid within the dimensions of a single pixel may be stirred and not molecularly mixed. To emphasize this point, we will refer to ξ_mix as the *stirredness*.

The scalar dissipation field and stirredness will be utilized in the current investigation to analyze the mixing state of the jet shear layer during vortex roll-up and pairing. The primary means of studying the state of molecular mixing, however, will come directly from two-dimensional images of the molecularly mixed jet fluid fraction obtained from the dual-tracer PLIF technique. This method is described in Sec. III.

III. DUAL-TRACER PLIF THEORY

A number of researchers have used PLIF to obtain time-resolved, two-dimensional images of concentration in a mixing layer.[36,37] In the passive scalar PLIF technique, the jet or co-flow fluid is seeded with a tracer such as Rhodamine[38,39] or disodium fluorescein[40] dye for liquid flow, and acetone for gaseous flow.[41] The detected LIF signal is linearly proportional to the tracer concentration. Such passive scalar PLIF studies have been used to obtain quantitative measurements of mixed fluid fraction, but the extent of *molecular* mixing is typically unknown since the smallest scales imaged are still much larger than the Batchelor scale at high Reynolds numbers. Measurements of molecular mixing can be obtained using high-resolution passive scalar PLIF;[31,32] however, the large-scale flow structures cannot be imaged simultaneously with this method. Combined acetone/OH PLIF has recently been demonstrated in jet diffusion flames[42,43] and reacting, compressible shear layers,[42,44] and a NO/OH PLIF system has also been developed for reacting, supersonic flows.[45] However, it is difficult to relate the fluorescence signal to flow field properties in such multiple scalar work.

In contrast to passive scalar PLIF, quantitative measurements of molecular mixing have been made using acid-base[3,40,46] or cold chemistry[47–49] ''flip'' experiments. Such flip experiments provide a statistical measurement of the *time-averaged* molecularly mixed fluid fraction.[47] In the dual-tracer technique developed by King *et al.*,[7,50] on the other hand, simultaneous passive scalar and cold chemistry tracers are used to provide *instantaneous* planar maps of molecular mixing in turbulent gaseous flows while simultaneously studying the large-scale turbulent structures. This technique is used in the current investigation and is briefly summarized below.

For uniform laser energy, optical collection efficiency, Einstein coefficient of absorption, and overall number density, a PLIF signal that is in the linear regime (weak laser excitation) and can be described by a two-level model, is directly proportional to the local mole fraction of seeded fluid, x_i, and the local fluorescence efficiency:

$$S_{f,i} \approx \frac{x_i A_i}{A_i + Q_i + K_i}, \tag{6}$$

where the fluorescence efficiency is composed of the Einstein coefficient for spontaneous emission, A_i, the collisional quenching rate, Q_i, and the upper-level loss rate due to collisionless processes, K_i.

Nitric oxide is termed a ''cold chemistry'' tracer because as it mixes at the molecular level with even a small amount of air, the LIF signal drops off dramatically due to quenching from oxygen.[48] For the case of a NO-seeded jet, therefore, the NO LIF signal, $S_{f,\mathrm{NO}}$, for a particular pixel is received almost entirely from jet fluid that is in the pure unmixed state. The fraction of *pure, unmixed* jet fluid within a pixel, f_{pjet}, is then found by[7,50]

$$f_{\mathrm{pjet}} = \frac{S_{f,\mathrm{NO}}(\text{mixing layer})}{S_{f,\mathrm{NO}}(\text{pure jet})}. \tag{7}$$

The remaining fluid within the pixel that is not pure jet fluid consists of either mixed jet fluid or co-flow fluid. Therefore, the cold chemistry tracer cannot by itself give the fraction of mixed fluid within a pixel because the fraction of co-flow fluid is unknown.

Acetone, on the other hand, is referred to as a ''passive scalar'' tracer because its collisionless loss rate is much larger than its collisional quenching rate due to nitrogen or oxygen, making its LIF signal nearly independent of the mixing state.[51] Assuming that the acetone is seeded into the co-flow fluid, the ratio of the acetone LIF signal for a pixel in the mixing layer to the LIF signal in the pure co-flow fluid will give the fraction of total co-flow fluid, f_{tcf}, within that pixel:[7,50]

$$f_{\mathrm{tcf}} = \frac{S_{f\mathrm{ac}}(\text{mixing layer})}{S_{f\mathrm{ac}}(\text{pure co-flow})}. \tag{8}$$

While this measurement of f_{tcf} can provide a picture of large-scale structure entrainment, it does not reveal any information about what occurs on the molecular level, since the fluids imaged within a pixel may not necessarily be mixed. By using simultaneous cold chemistry and passive scalar images, on the other hand, the fraction of molecularly mixed jet fluid can be found from

$$f_{\mathrm{mjet}} = f_{\mathrm{tjet}} - f_{\mathrm{pjet}} = 1 - f_{\mathrm{tcf}} - f_{\mathrm{pjet}}. \tag{9}$$

Furthermore, a mixing efficiency can be defined to measure the ratio of molecularly mixed jet fluid to the total jet fluid within each pixel:

$$\eta_{\mathrm{mix}} = \frac{f_{\mathrm{mjet}}}{f_{\mathrm{tjet}}} = \frac{1 - f_{\mathrm{tcf}} - f_{\mathrm{pjet}}}{1 - f_{\mathrm{tcf}}}. \tag{10}$$

Values of $\eta_{\mathrm{mix}} = 0$ indicate pure co-flow or pure jet fluid, values of $\eta_{\mathrm{mix}} = 1$ indicate regions that are completely mixed at the molecular level, and values of $0 < \eta_{\mathrm{mix}} < 1$ indicate the existence of pure fluid structures that are smaller than the imaging resolution (i.e., subresolution stirring).

An additional benefit of obtaining the fraction of co-flow air from the acetone signal is the ability to incorporate a finite-rate chemistry model into the image processing methodology. A theoretical plot of the normalized NO LIF signal as a function of the total co-flow fluid fraction is shown in Fig. 1, and is based on Eq. (6) and quenching-rate correlations from Eckbreth[37] and Paul *et al.*[52] Due to its large quenching cross-section relative to oxygen, the presence of acetone at the seeding level of the current investigation (4.6% by mass) increased the NO LIF quenching rate by about 50%. Due to the non-negligible NO LIF signal present at low air concentrations, the fraction of mixed jet fluid calculated from the experimental results was adjusted such that

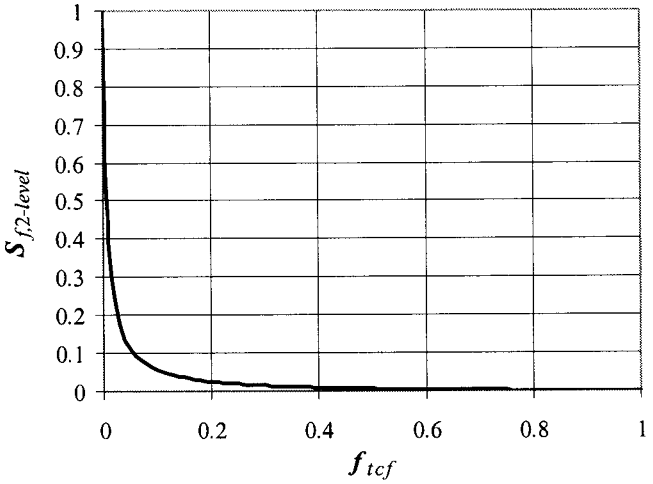

FIG. 1. Theoretical calculation of the normalized NO LIF signal from the two-level model as a function of the total co-flow fluid fraction. Quenching rates are calculated assuming seeding densities of 300 ppm for the NO-in-N_2 jet and 4.6% by mass for the acetone-in-air co-flow.

$$f_{\mathrm{mjet}}=\frac{1-f_{\mathrm{tcf}}-f_{\mathrm{pjet}}}{1-S_{f,\text{two-level}}}, \tag{11}$$

where $S_{f,\text{two-level}}$ is the normalized NO LIF signal predicted from the two-level model of Eq. (6) and is shown as a function of f_{tcf} in Fig. 1.

IV. EXPERIMENTAL TECHNIQUE

The experimental facility used in this study is shown schematically in Fig. 2. The jet fluid consists of ultrahigh purity N_2 seeded at 280–300 ppm with NO and regulated by Tylan mass flow controllers with ±1% full-scale accuracy and ±0.2% full-scale repeatability. After entering the Plexiglas™ speaker chamber, the jet fluid is fed into a 21.5-mm-diam vertical tube which contracts to a 5-mm-diam nozzle designed for a top-hat jet exit velocity profile.[53] All experimental data for the current investigation were obtained at an area- and time-averaged jet exit velocity of 6.7 m/s ($\mathrm{Re}_D=2300$). A 25.4-cm-diam loud speaker (Pyle Driver HW 1070) is used to create an acoustic pulse that causes a vortex to form in the jet shear layer. The transient jet exit velocity which results from the acoustic pulse is measured with a 20-μm-diam, 1-mm-long hot-wire filament.

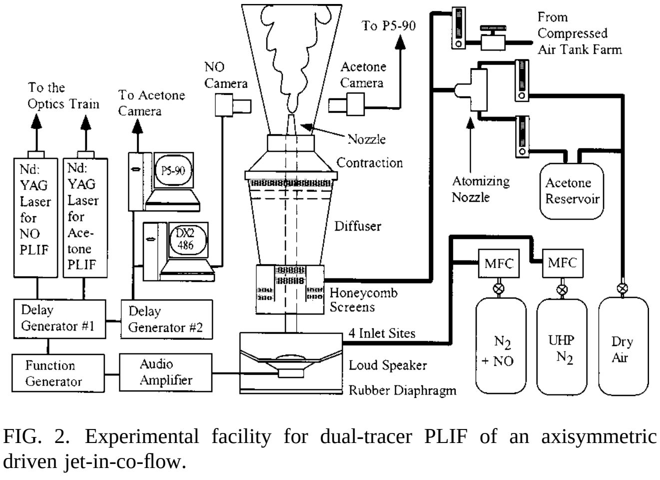

FIG. 2. Experimental facility for dual-tracer PLIF of an axisymmetric driven jet-in-co-flow.

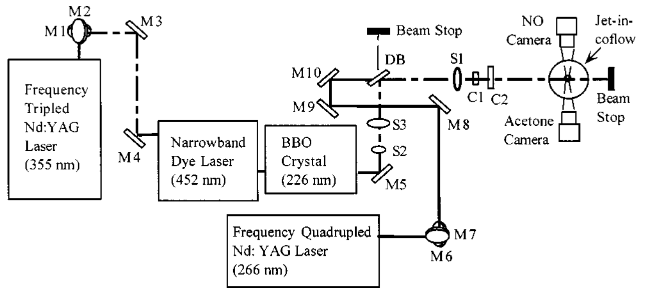

FIG. 3. Layout of dual-tracer PLIF lasers and optics. M1–M4: 355 nm mirrors. M5: 226 nm mirror. M6–M10: 266 nm mirrors. S1: $f=+1$ m spherical lens. S2: $f=-50$ mm spherical lens. S3: $f=+100$ mm spherical lens. C1: $f=-19$ mm cylindrical lens. C2: $f=+150$ mm cylindrical lens. DB: dichroic beamsplitter.

The co-flow fluid consists of air at 12 SCFM (0.27 m/s) seeded with acetone at 4.6% by mass. Acetone seeding is accomplished using a stainless steel atomizing nozzle that is located about 10 m upstream of the diffuser inlet to allow enough time for vaporization and uniform mixing. The seeded air is passed through five honeycomb rings and two mesh screens that are located in an annular diffuser section before exiting through a 16-cm-diam circular opening. The entire jet-in-co-flow apparatus is mounted on a three-axis translation system that can be moved with 2.54 μm resolution.

Figure 2 also shows the timing electronics used in the experiment. A Stanford Research Systems function generator (SRS-DS345) is used as the master timing device, triggering the speaker pulse and laser *Q*-switching events. The function generator creates a 20 Hz wave form with a sharp leading edge, a 2 ms plateau, a 10 ms ramp down, and a 38 ms delay period. This wave form is sent to the audio amplifier (Optimus STA-900) which powers the loud speaker. Delay generators 1 and 2 (Stanford Research Systems DG535) are used to ensure that the 10 Hz laser pulses arrive at the probe volume simultaneously (to within 5 ns) and to ensure that they are phase locked to the cameras and to the acoustic pulse.

A schematic of the dual-tracer PLIF lasers and optical components used in this study is shown in Fig. 3. While the excitation wavelengths of NO and acetone are both in the ultraviolet, they are sufficiently separated to require two laser excitation sources. A frequency-quadrupled (266 nm) Nd:YAG laser (Continuum PL-8010) is used for acetone excitation, which peaks from 270 to 280 nm.[51] A 226 nm beam is used for excitation of the NO γ band $[A\,^2\Sigma^+\leftarrow X^2\Pi(0,0)]$ transition. To obtain the 226 nm beam, a frequency-tripled (355 nm) Nd:YAG laser (Continuum NY 81 C-10) is used to pump a tunable, narrowband dye laser (Lumonics HD-300 with Coumarin 450 dye in methanol) to produce a 452 nm beam. A second harmonic generator containing a beta-barium borate (BBO) crystal is then used to generate the 226 nm beam. Typical laser energies are

130 mJ for the 266 nm beam and 0.5 mJ for the 226 nm beam.

Figure 3 also shows the optical components required to obtain co-planar laser sheets. The beam-expanding telescope (S2 and S3) is used to translate the focal point of the 226 nm laser beam independently of the 266 nm beam. A long-wave pass dichroic beamsplitter (DB) is then used to combine the two beams. Finally, the spherical focusing lens (S1) and two cylindrical lenses (C1 and C2) are used to form laser sheets that are 200–300 μm thick and 2.5 cm high.

PLIF images are captured with two Photometrics Ltd. 512×512 pixel array, 14 bit digital charge-coupled device (CCD) camera systems (with pixel center-to-center spacing of 27 μm). IBM-compatible personal computers control the exposure settings and store the images for each camera. A Nikkor 50 mm glass lens with a lens-mount adapter (to increase magnification) is used for the acetone camera. An $f\sharp$ of 1.2 is used to improve the signal-to-noise ratio (SNR), and the glass lens blocks the strong ultraviolet NO LIF signal. As shown in Fig. 3, the camera used for NO PLIF is located on the opposite side of the jet, and is fitted with a lens-mount adapter and as UV Nikkor 105 mm multielement lens (composed of quartz and fluorite). The lens $f\sharp$ of 4.5 reduces the relatively weak acetone LIF signal to about 5% of the NO signal. This residual acetone signal is subtracted from the NO PLIF images during image processing.

Based on Eq. (2) and the results of Buch and Dahm[32] in a turbulent gaseous jet, the smallest possible diffusion length scales for the flow conditions of this study range from 90 to 260 μm. Calculated assuming homogeneous turbulence, this range represents a lower limit of the imaging resolution required for the well-organized, axisymmetric structures expected in the jet near field of the current investigation. This range of diffusion scales further indicates that the imaging system described above (with flow field resolution $\Delta x = \Delta y = 50.7\,\mu$m) is at least 1.8–5 times oversampled. The two-dimensional nature of the large-scale structures also ensures that the laser sheet thickness (200–300 μm) adequately resolves scalar gradients in the azimuthal direction.

In addition to evaluating the pixel resolution relative to the smallest possible diffusion length scales, it is also important to consider systematic errors in various components of the imaging system. A means of evaluating the limiting resolution due to such errors is described by Paul *et al.*,[22] and is based on the pixel-to-pixel spacing, image magnification, focal length, lens $f\sharp$, focusing error, and Nyquist criterion. Based on this analysis, the smallest length scales that the imaging system can faithfully record are greater than approximately 190 μm. Thus, the current resolution may not fully resolve the concentration gradients required for an accurate calculation of scalar dissipation. While this is of particular concern further from the optical axis of the camera lens, vortex pairing events and correspondingly large scalar gradients occur primarily in the central one-third of the imaging region. A more detailed evaluation of sampling error in the measurement of scalar gradients will be presented in the discussion of experimental results.

For a two-camera experiment, image registration is also extremely important to ensure spatial correlation between the two fluorescence images. After rough camera registration in ambient light, a set of registration images is obtained using a spray of acetone droplets into the laser sheets. Scattered laser light is imaged by the NO camera, while the acetone droplet fluorescence is captured on the second camera. Registration points are then obtained from the locations of the smallest available droplets in each image. These registration points are used to generate conformal mapping coefficients from a least-squares fit, and to transform the scale and orientation of the acetone PLIF image pixel coordinates (to those of the NO image) using bilinear interpolation. When the initial camera registration in ambient light is performed carefully, conformal remapping results in a spatial mismatch of less than 1 pixel. This can be verified by comparing the peak signal locations of the registration points from various regions of the original NO and remapped acetone PLIF images.

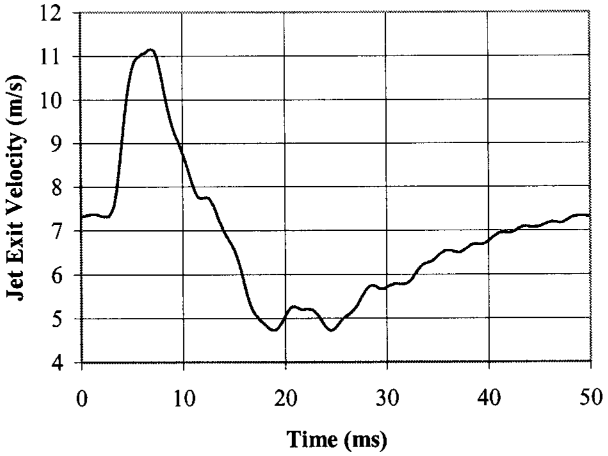

FIG. 4. Jet exit centerline velocity during the 50 ms time period between acoustic pulses.

After image registration, average backgrounds are subtracted from each image to eliminate any repeatable beam scattering. The background-subtracted acetone images are then used to eliminate the residual acetone signal (~5%) from each NO PLIF image. Acetone images are corrected for beam attenuation using an absorption coefficient calculated from a least-squares fit to Beer's law in a region of uniform acetone concentration. Both the acetone and NO images are also normalized to account for laser sheet-intensity and camera-response variations. The typical SNR of the normalized and corrected images is 40:1 for both the acetone and NO PLIF.

V. RESULTS AND DISCUSSION

A. Jet response to acoustic pulsing

Velocity data were obtained from hot-wire measurements to establish the boundary and excitation conditions for the stable vortex pairing events generated in the current investigation. The time-dependent jet exit centerline velocity resulting from the 20 Hz acoustic pulse is shown in Fig. 4, which is an average of 20 time traces taken from hot-wire data. The transient velocity follows the trend of the driving wave form, but the acoustic pulse arrives at the jet exit ap-

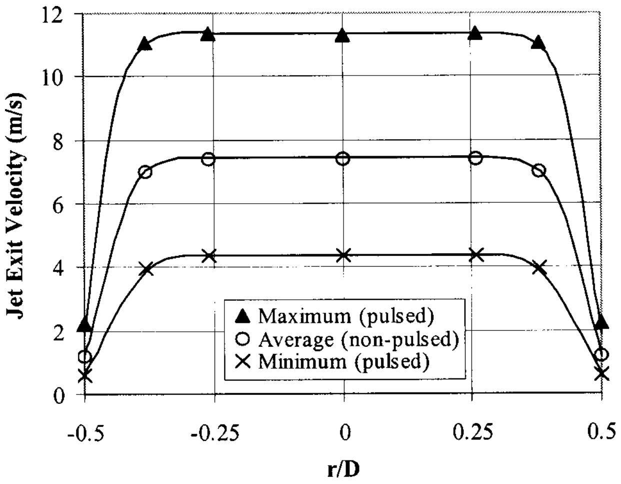

FIG. 5. Radial variation of jet exit velocity showing a nearly top-hat profile for both pulsed and non-pulsed conditions.

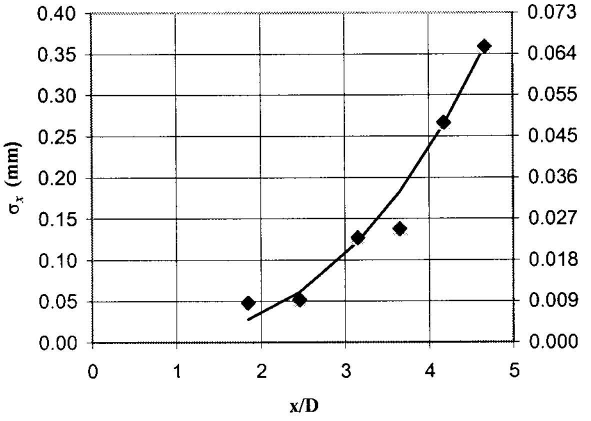

FIG. 7. Shot-to-shot variability of vortex locations and timing plotted as a function of axial distance from the jet exit ($\sigma_{\text{time}} = \sigma_x / V_{\text{conv}}$).

proximately 3 ms after the electronic trigger. This is due to the finite response time of the speaker chamber (0.7 ms) and the time it takes the acoustic pulse to reach the jet exit (2.3 ms). The velocity undershoot from about 10 to 40 ms injects vorticity of the opposite sign into the shear layer, although no PLIF data were taken during this latter period. Figure 5 shows jet exit radial velocity profiles when the jet issues into still air. The jet exit velocity is nearly top-hat for both pulsed and nonpulused conditions. The radial co-flow velocity profile near the jet exit is available from previous hot-wire measurements in the same jet facility, and shows no evidence of separation of the nozzle exterior.[23]

The time-dependent jet centerline velocity was also measured at two locations downstream of the nozzle exit to determine the effect of acoustic pulsing. In comparison with the steady jet, which maintains its centerline velocity constant to within 0.4% at $x/D=4$, the pulsed-jet time-averaged centerline velocity decreases by 2% at $x/D=2$ and by 4% at $x/D=4$ due to increased shear layer entrainment. The transient centerline velocity for a portion of the 50 ms time period is shown in Fig. 6 at three axial locations. The velocity profile at $x/D=0.2$ is upstream of any vortex formations, and indicates that the jet exit centerline velocity is nearly constant from 5.5 to 7.5 ms after the acoustic pulse. All PLIF images fall within the 4.4–8.6 ms time period, during which the jet exit velocity varies by less than 12%. The velocity profile at $x/D=2$ shows a series of double peaks indicating that the passage of two closely spaced vortices occurs regularly at this location. Further downstream at $x/D=4$, a series of single peaks indicates that the vortices that were present at $x/D=2$ have merged.

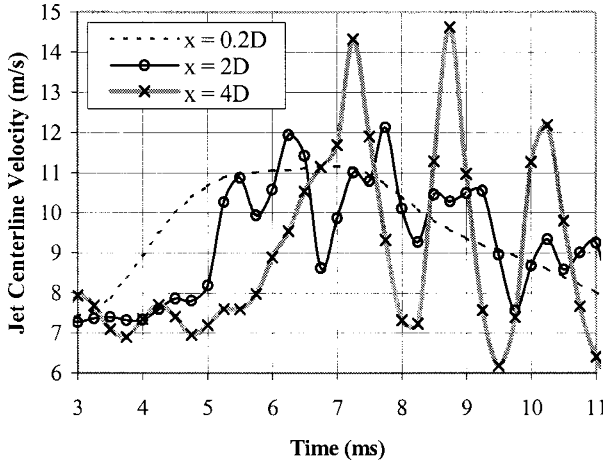

FIG. 6. Jet centerline velocity as a function of time after the acoustic pulse for different axial locations.

The large velocity fluctuations shown in Fig. 6 at $x/D=4$ indicate that the merged structures have increased significantly in size, thereby reducing the local jet core diameter. The Strouhal number at this location, $\text{St}_D = fD/U_{\text{exit}}$ is about 0.30 based on the frequency (~660 Hz) of these large amplitude fluctuations. This is often referred to as the Strouhal number of the preferred mode,[1,25] and has been found in previous investigations to vary from 0.30 to 0.50.[1,20,25] The Strouhal number of the driven vortices upstream of the pairing event ($\text{St}_D=0.60$) agrees, as expected, with the Strouhal number of the free shear layer initial instability. Thus, the broadband acoustic pulse interacts with and amplifies the most unstable mode of the axisymmetric jet through the higher harmonics of its 20 Hz driving wave form.

Natural instabilities become fairly significant, however, after only a few jet diameters downstream of the nozzle exit. This limits the ability to correlate the movement of vortices in a phase-locked sequence of hot-wire measurements or PLIF images. The transient jet velocity is repeatable to within 0.5% near the nozzle exit, for example, but only to within 3% at $x/D=4$. To quantify the limiting temporal resolution due to natural instabilities, the shot-to-shot variability of vortex arrival times was measured from dual-tracer PLIF images. The results are plotted in Fig. 7 and show that the timing jitter is less than 0.01 ms near $x/D=2$. Vortices near $x/D=4$ have a timing jitter of about 0.04 ms and are, therefore, less correlated in time. Phase averaging was avoided because it smears the scalar spatial gradients. The maximum timing error at all measurement locations was reduced to about 0.01 ms by selecting instantaneous images that most closely matched the phase-averaged vortex positions.

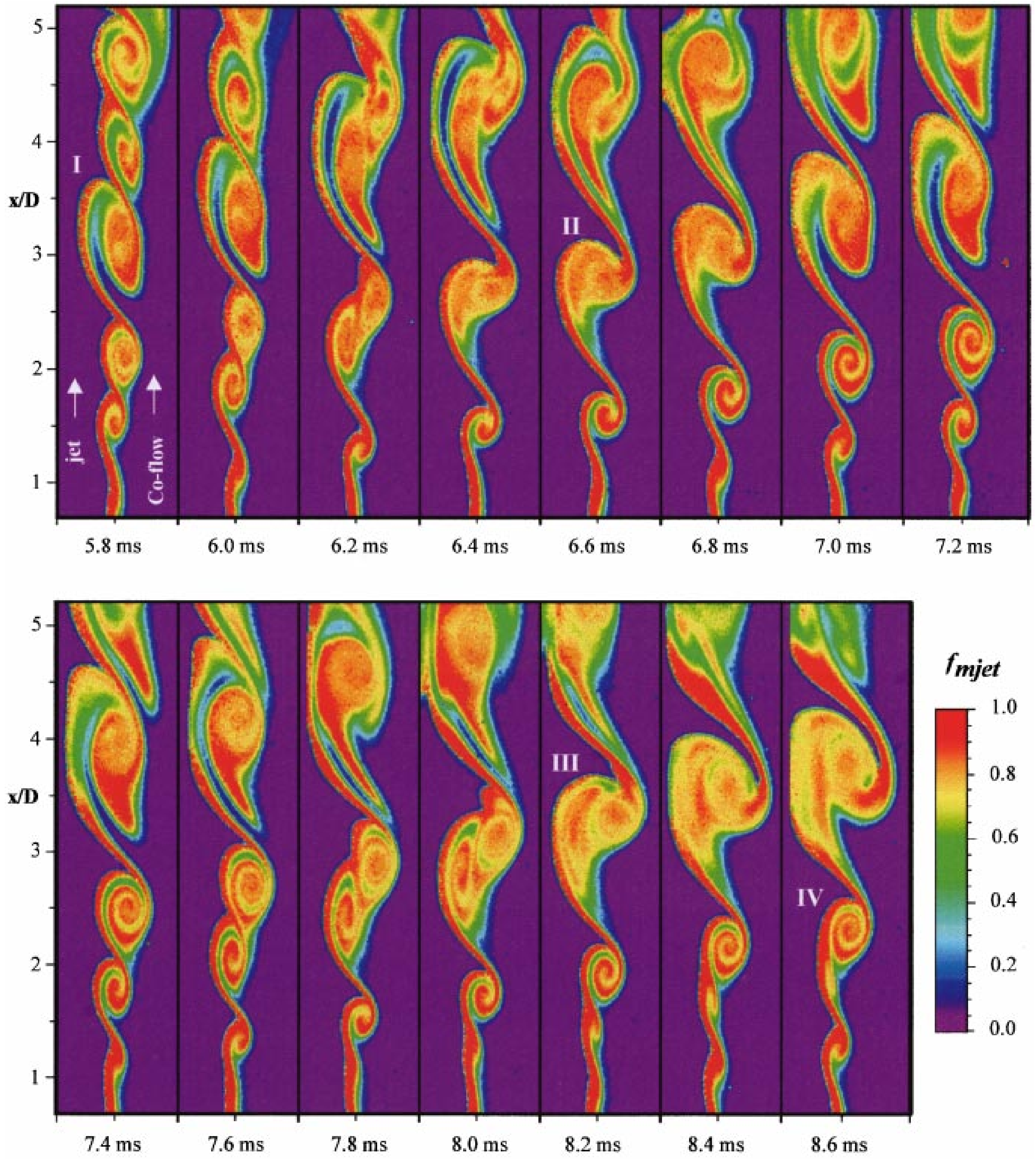

FIG. 8. Instantaneous maps of molecularly mixed jet fluid fraction, f_{mjet}, from 5.8 to 8.6 ms after the acoustic pulse. Each image spans an axial distance of $0.7<x/D<5.2$ and the bottom scale is $0<r/D<1$. The symbols I–IV refer to different pairing events.

B. Vortex dynamics

Although vortex formation and interaction have been studied in previous investigations,[2,20] further insight is made possible by the improved spatial and temporal resolution of the current work. In addition, it is useful to summarize dynamical aspects of the pairing process for reference in subsequent discussions that pertain more specifically to scalar mixing.

A sequence of instantaneous half-jet images of mixed jet fluid fraction, f_{mjet}, from the dual-tracer PLIF technique is shown in Fig. 8. The time spacing is 0.2 ms, and the time span ranges from 5.8 to 8.6 ms after the speaker pulse. The passage of closely spaced vortices near $x/D=2$ and paired vortices near $x/D=4$ confirm the results of the hot-wire velocity measurements discussed above. In order of occurrence, the sequence of images includes a postpairing structure (labeled I), a nearly complete sequence for two pairing events (labeled II and III), and a prepairing roll-up (labeled IV). The observable stages of pairing include vortex roll-up, interaction, coalescence, and re-entrainment.

Figure 8 shows the roll-up of a single vortex beginning at the very bottom of the image obtained at 5.8 ms after the speaker pulse. This is the leading vortex of the pairing event labeled III. The initial instability is axisymmetric rather than helical, and is characteristic of jet instabilities at Reynolds numbers on the order of $\mathrm{Re}_{\mathrm{jet}} = 1000$ and higher.[1] According to the classical description of vortex formation in liquids,[2] a small amplitude wave distorts the constant vorticity shear layer, inducing cross-stream velocities that cause the disturbance to grow. The disturbance then becomes organized into a thick region of vorticity that eventually pinches off from the vorticity-depleted braid region to form a discrete vortex. The mechanism shown in Fig. 8 seems to follow a similar pattern, as indicated by the images from 5.8 to 6.2 ms.

The entrained layers of jet and co-flow fluid for the leading vortex of pairing event III during the roll-up from 6.2 to 7.0 ms are almost entirely molecularly mixed, with a jet-to-co-flow fluid entrainment ratio of almost 4:1. Measurements indicate that the vortex width grows linearly during this period. At 7.2 ms, however, the approach of a trailing vortex has clearly begun to interfere with co-flow fluid entrainment and marks the beginning of vortex interaction. By 7.4 ms, the leading vortex ceases to grow and is pushed away from the jet centerline. During this stage, the entrainment of vortical fluid from the braid region is also interrupted, which explains the threefold drop in the vorticity of the leading vortex observed by Hussain and Zaman[13] during the same time period.

The effect of this vortex interaction on the trailing vortex is somewhat delayed since it is free to entrain co-flow fluid and grow in size until about 7.8 ms. At this point, the braid region between the two vortices is completely engulfed and the trailing vortex moves significantly closer to the jet centerline. The end of fluid entrainment and vortex growth at about 7.8 ms is in accordance with the measurements of Hussain and Zaman,[13] who found that the trailing vortex maintains its vorticity up until this point, and then the vorticity drops by over 50% soon thereafter.

The time period after 7.8 ms marks the beginning of vortex coalescence. Following the convention of Ho and Huang,[54] the actual pairing event (labeled III) is defined at 8.2 ms where the two vortices are at the same axial location. The gross stretching and deformation of the diffusion layers indicates the onset of large-scale turbulence and rapid homogenization.

The following discussion of the postpairing structure now shifts to pairing II, which occurs at 6.6 ms and is qualitatively similar to pairing III discussed above. The entrainment of jet and co-flow fluid by the paired structure begins before coalescence is complete and continues from 6.6 to 7.6 ms. A large amount of unmixed co-flow fluid is pulled deep into the merged structure, and most of the newly entrained jet fluid collects at the trailing edge. The lack of rotation of this structure causes a ‘‘kinked’’ or ‘‘comma-shaped’’ configuration rather than the classic spiral of a typical vortex roll-up. By 7.8 ms, no further jet fluid entrainment takes place and molecular diffusion slowly eliminates the layers of pure fluid.

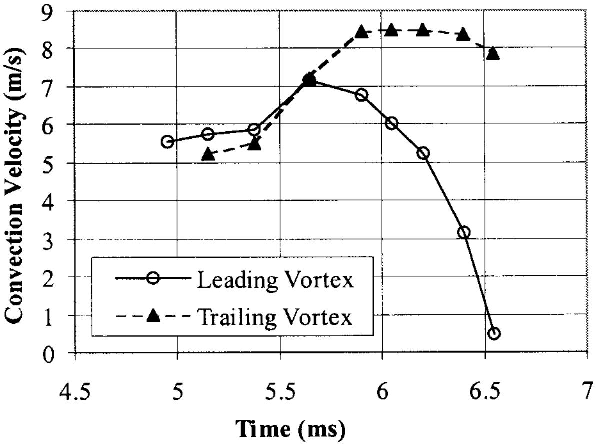

FIG. 9. Vortex convection velocities of pairing II from 4.9 to 6.6 ms after the acoustic pulse.

A variation of the re-entrainment process is shown from 5.8 to 7.0 ms, when the postpairing structure of pairing I merges with an isolated vortex. This merging process is quite different than the merging of two isolated vortices discussed earlier. Co-rotation is hampered by the size of the paired structure and coalescence of the core regions never takes place. The merging event generates sufficient rotation, however, for renewed co-flow entrainment (see image at 7.0 ms).

The effect of pairing on vortex convection velocity is shown in Fig. 9. The time period encompassing pairing II was used because the jet exit velocity is approximately constant (see Fig. 6) and has a minimal effect on the vortex behavior. The uncertainty of the convection velocity data is typically 13%–17% due to first-order finite differencing and shot-to-shot timing jitter, but several trends are apparent in the results. Prior to vortex interaction, the convection velocities are about one-half the jet exit velocity of 11 m/s during this period and are increasing slightly. The beginning of vortex pairing is indicated by a marked increase in the convection velocities of *both* vortices after about 5.4 ms. A similar trend is reported by Zaman and Hussain,[20] but the reason for this behavior is not well understood and may require more detailed velocity measurements. It can be surmised from the dual-tracer PLIF images, however, that vortex co-rotation and re-entrainment from the pairing event occurring downstream may increase the local convection velocity further upstream. After this initial acceleration, the leading vortex begins to decelerate from 5.6 to 6.6 ms. The velocity drops very substantially down to about 0.5 m/s as it is cut-off from the jet core, undergoes co-rotation with the trailing vortex, and moves radially outward. The velocity of the trailing vortex, on the other hand, continues to increase from 5.6 to 5.8 ms as it moves closer to the jet centerline. The trailing vortex then remains at a constant velocity from 5.8 to 6.4 ms, indicating that although it is moving closer to the jet centerline, it is in the top-hat region of the jet core. The convection velocity of 8.4 m/s during this period is 25% above the area- and time-averaged jet exit velocity of 6.7 m/s and matches the excess velocity reported by Zaman and Hussain.[20] At about 6.6 ms, however, the trailing vortex begins to decelerate due to co-rotation with the leading vortex. Thus, the vortex convection velocity data confirm the existence of various stages of vortex pairing, including vortex roll-up, interaction, and co-rotation/coalescence. The re-entrainment stage is not shown in Fig. 9 because of the difficulty in defining the center of the merged structure, but the postpairing convection velocity can be estimated from the PLIF images and hot-wire data at $x/D=4$ to be about 6–7 m/s.

C. Mixed jet fluid fraction and mixing efficiency

As noted earlier, passive scalar measurements of fluid concentration have been found to overestimate the fraction of molecularly mixed fluid due to limitations on spatial resolution.[5,27] Because this investigation is concerned with measurements of molecular mixing in large-scale structures that are undergoing significant deformations, it is useful to determine if subresolution stirring can be detected. This would indicate the existence of small-scale structures and aid in the interpretation of mixing data. From Eq. (10), regions of subresolution stirring are identified by nonunity values of the mixing efficiency.

Figure 10 shows images of mixed jet fluid fraction, f_{mjet}, and mixing efficiency, η_{mix}, at 6.6 ms after the speaker pulse (for a different instantaneous image than that shown in Fig. 8). The line plots of column 1 and row A refer to vertical and horizontal cross-sections, respectively, of co-flow fluid that has been engulfed into a postpairing structure. Values of $f_{\mathrm{mjet}}\approx 0.2-0.3$ indicate that jet fluid has had enough time to diffuse into this region, and values of $\eta_{\mathrm{mix}}\approx 1.0$ indicate that nearly all this jet fluid is mixed at the molecular level.

Row B shows a cross-section of pairing event II. The mixed jet fluid fraction for this region ($f_{\mathrm{mjet}}\approx 0.8$) is indicative of the entrainment ratio for the shear layer. The individual vortices are still barely discernible, but the composition does not ramp across the shear layer at this location. A high value of f_{mjet} is shown at the edges of the cross-section, however, where the rotation from the pairing event causes the entrainment of new jet fluid. Note that the mixing efficiency in row A also remains at approximately unity for almost the entire pairing structure, indicating that the jet fluid is *molecularly* mixed. This is an important result because it indicates that the mixing process during the pairing event takes place through large-scale deformation of the vortex layers, and that the subsequent cascade of scales prior to molecular diffusion does not reach subpixel dimensions.

The fractional uncertainty in the experimental results is typically about 4% for both f_{mjet} and η_{mix}, but can be as high as 20% in regions of low jet fluid fraction. Thus, the plots of f_{mjet} and η_{mix} have significant fluctuations in the co-flow engulfment regions sectioned by column 1 and row A, though the trend toward $\eta_{\mathrm{mix}}\approx 1.0$ (molecularly mixed) structures is evident in regions of both high and low uncertainty. Differential diffusion is another factor that may affect the detection of subresolution stirring. The binary diffusion coefficient of acetone in nitrogen or air is about one-half that of oxygen in nitrogen or air, which limits the ability of acetone to act as an accurate tracer for the co-flow air. However, previous studies have shown that differential diffusion of oxygen is a concern in measurements of η_{mix} only for regions of low air concentration ($f_{\mathrm{tcf}}<0.05$).[7,27] This is primarily due to the quenching rate of the NO LIF signal shown previously in Fig. 1, which is strongly affected by a slight increase in the presence of oxygen for regions of low air concentration.

D. Stirredness

Plots of molecularly mixed jet fluid fraction provide instantaneous two-dimensional views of the state of molecular mixing within the shear layer. Stirredness, on the other hand, provides a measure of the uniformity of the fluid structures. This is useful for quantifying the evolution of the internal vortex structure at various stages of the pairing event. In particular, the existence of a viscous core region is important for modeling purposes.[55] Furthermore, since the jet fluid in the core region is almost entirely molecularly mixed ($\eta_{\mathrm{mix}}\approx 1$), stirredness calculations provide a good measure, scaled from 0 to 1, of how close the region is to reaching a uniform, area-averaged jet mixture fraction.

According to Eq. (5), stirredness is an area integral. Because the area of the core region of a vortex roll-up changes with time, it was not possible to track the evolution of stirredness for a region of fixed area. In addition, determining the size of the core region presented a difficulty, since the stirredness is not a function of the spatial coordinates. For these reasons, stirredness was calculated using a series of concentric rings as shown in Fig. 11. The innermost ring is a circle centered within the vortex and should be the most homogeneous region of the vortex roll-up. Each additional concentric ring is more likely to encounter pure co-flow or pure jet fluid. Thus, the stirredness should decrease as a function of the concentric ring diameter. If a homogeneous core region exists, however, the stirredness should remain fairly constant for increasing ring diameters that are within the vortex core. This procedure can be used to determine the size of the homogeneous core region of a vortex from the initiation of instability and through the pairing event. This procedure is attractive from a data processing perspective, although a consistent selection of vortex center locations is required. Since the location of peak vorticity was not available for the current investigation (no velocity data), the vortex center was chosen to be the midpoint of the line which connects the innermost points of the jet and co-flow entrainment layers (Fig. 11). When a clear view of these inner layers is obscured by scalar diffusion, the approximate center was determined using line plots across the core region. Of course, the size of the core region can also be estimated directly from these line plots, but noise in the data would limit the ability to detect subtle changes in size and composition.

Figure 12 shows a plot of stirredness as a function of the concentric ring outer diameter for all stages of development for the leading vortex of pairing III (Fig. 8). The first indication of the vortex roll-up occurs at 6.2 ms after the speaker pulse. The stirredness drops immediately for each subsequent concentric ring at this time, indicating that if a homo-

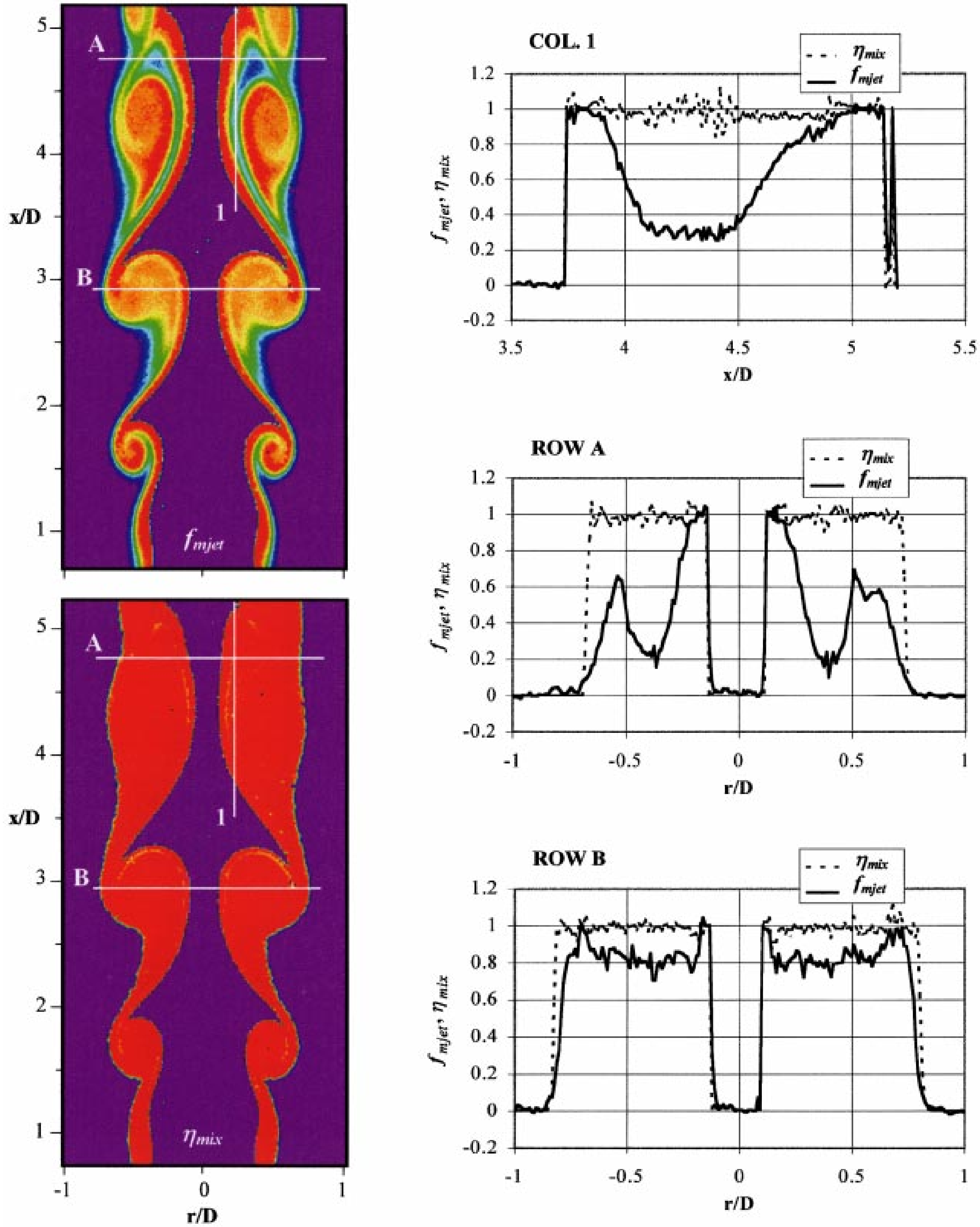

FIG. 10. Instantaneous maps and line plots of molecularly mixed jet fluid fraction, f_{mjet}, and mixing efficiency, η_{mix}, 6.6 ms after the acoustic pulse. The color scale is shown in Fig. 8.

geneous core region exists, it is smaller than the minimum measurement diameter (6 pixels or about 300 μm). An increase in the initial negative slope of the curves seems to occur starting at about 7.0 ms. Another increase is seen at 7.4 ms, clearly indicating that there is a significant homogeneous core region. From this point forward, the size of the core region grows continually to a size of almost 0.4 D. Note that the value of stirredness is at about 0.99 for these later times, indicating that noise in the calculations does not cause an underestimate of the uniformity within the core region. Results are not presented here for the trailing vortex because large deformations during the pairing event did not allow the

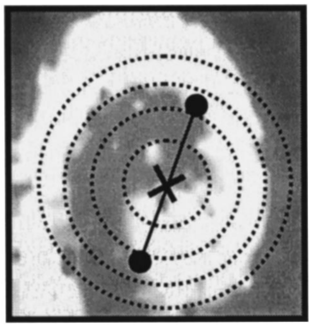

FIG. 11. Definition of the vortex core center and relative spacing of concentric regions used for stirredness calculations. Area shown is 0.2 D ×0.2 D.

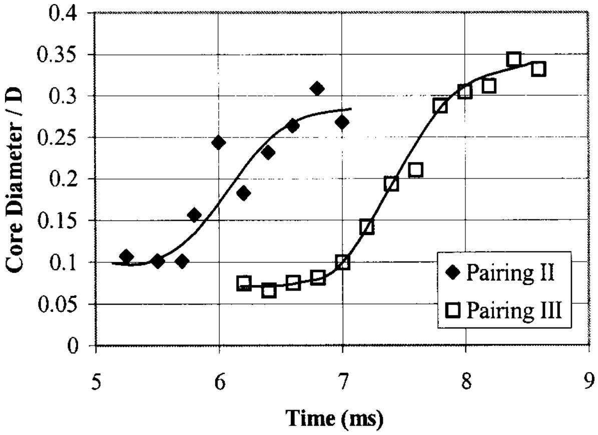

FIG. 13. Core diameter as a function of time for the leading vortex of pairings II and III.

use of a well-defined geometry for area averaging. The core region is also difficult to distinguish during the stretching phase of pairing for the trailing vortex.

Of additional interest in the current investigation is the manner in which the size of the core region changes at different stages of vortex evolution and pairing. From the data of Fig. 12, the size of the core region was calculated as a function of time. The core region was defined to include concentric ring diameters in which the stirredness was within 99% of the center value. This allowed the diffuse remnants of the leading vortex cores to be distinguished for an evaluation of the trends during and after the pairing event. Figure 13 compares the results for pairing events II and III. Note that for both pairing events, the core diameters remain fairly constant in the early stages of roll-up. The finite core diameters during this time are a result of the 99% selection process, however, and are not necessarily meaningful where homogeneous regions are not detected. At about 5.7 ms for pairing II and 7 ms for pairing III, the size of the core region increases dramatically. As discussed earlier, this is the stage of the pairing process in which the trailing vortex is approaching and beginning to interfere with the co-flow entrainment process of the leading vortex. It is also the stage at which Hussain and Zaman[13] reported a factor of 3 drop in the peak vorticity of the leading vortex, coupled with a significant increase in the core diameter of the vorticity contours. After this approach period, however, they found that the vorticity of the leading vortex for the rest of the pairing process decreases only slightly. Thus, it may be inferred from Fig. 13 that the end of this approach period and the beginning of vortex coalescence occurs near 6.5 ms for pairing II and near 8 ms for pairing III. This agrees with the trends in vortex growth and convection velocity discussed earlier and indicates that the changes in vorticity during vortex roll-up, interaction, and coalescence closely parallel the evolution of the mixing state.

Another means of tracking the effect of pairing on the mixing state is to measure the overall stirredness in a continuous region encompassed by both pairing vortices. This is shown in the plot of Fig. 14 for pairing event III. In typical studies of laminar vortex rings, the stirredness is found to

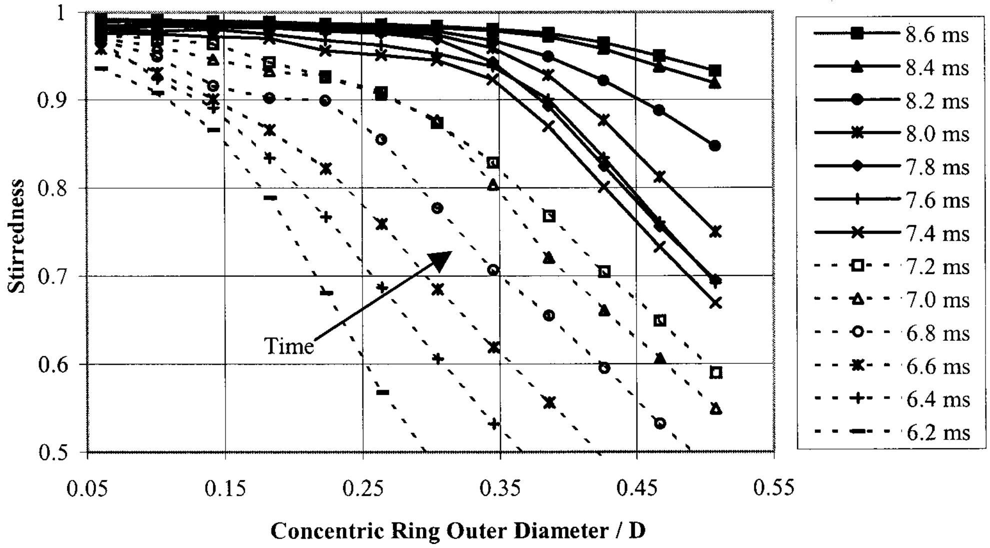

FIG. 12. Stirredness of the leading vortex for pairing event III plotted as a function of the outer diameter of the concentric measurement rings for different instants in time.

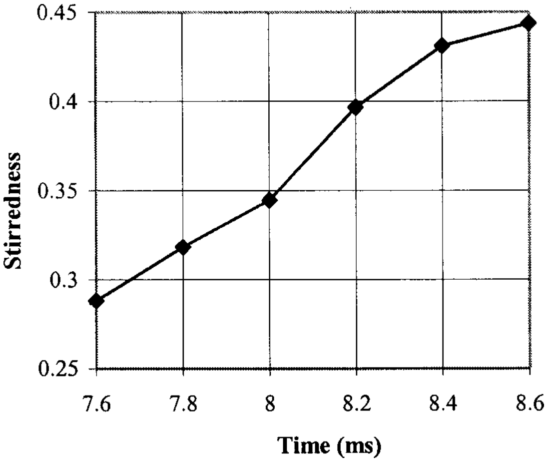

FIG. 14. Stirredness as a function of time for both vortices of pairing III.

increase linearly with time for a vortex of a given circulation.[35] This also seems to be the case for the vortices of pairing event III, even during the approach phase. The overall stirredness does not seem to be affected by the changes in the core region shown earlier in Figs. 12 and 13, but is a function of the overall vortex growth. A slight deviation from linear behavior is apparent in Fig. 14, however, from 8.0 to 8.6 ms. As shown previously in Fig. 8, these times include the period of vortex coalescence as well as the beginning of jet and co-flow re-entrainment.

E. Scalar dissipation

The sudden appearance of a homogeneously mixed core region has so far been explained by the interruption of co-flow fluid entrainment into the leading vortex as the trailing vortex approaches. The work of Flohr and Vassilicos,[55] however, indicates that it could also be due to accelerated scalar dissipation as the spacing of layers in the inner core is reduced by the roll-up process. Scalar dissipation, defined as $\nabla C_{\text{jet}} \cdot \nabla C_{\text{jet}}$ for the current investigation, is a measure of the rate of molecular mixing.[11,31] Since the driven vortices in the jet near field of the current investigation are nearly axisymmetric (see Fig. 10), the scalar dissipation field can be calculated using two-dimensional central differencing of the concentration field.

Figure 15 shows the scalar dissipation layers for the leading vortex of pairing III at 7.2 ms after the speaker pulse. The line plot illustrates the large difference in the magnitude of scalar dissipation between the inner and outer layers. For this reason, a logarithmic scale is used in the gray-scale image in order to view the scalar dissipation layers within the vortex core. The highest value of scalar dissipation is in the braid region ($r/D \approx 0.77$) due to the high strain rates, followed by the co-flow entrainment region ($r/D \approx 0.38-0.43$). Scalar dissipation is not as high in the jet entrainment region ($r/D \approx 0.72$) because of the high fraction of jet fluid that is already present in the vortex.

In order to evaluate the effectiveness of the imaging system, the scalar dissipation field was computed after artificially degrading the resolution using 2×2 pixel binning. A corresponding line plot of dissipation for the binned case is shown for comparison in Fig. 15. The average total dissipation from several binned images was computed over the entire flow field, and was found to capture a significant fraction (0.87 ± 0.02) of the average total dissipation from nonbinned images. Based on a similar study by Dahm *et al.*,[56] this indicates that the current imaging system is approximately 4× oversampled, and that the nonbinned images capture about 90%–95% of the actual total dissipation.

This resolution, therefore, seems adequate to capture the main qualitative trends of the diffusion layers in the current flowfield. The evolution of the instantaneous scalar dissipation field, shown in Fig. 16, reveals additional details about the mixing state of the pairing vortices. The vortices of pairing event III are shown at the bottom of the image at 6.8 ms. The trailing vortex is in the early stages of roll-up, visible only as a break in the scalar dissipation layer. This break indicates that the roll-up process begins with an incursion of co-flow fluid into the shear layer even prior to the pinching-off process described earlier in Sec. V B. No dramatic changes in scalar dissipation occur from 6.8 to 7.2 ms, but a slight break in the bottom layer of the leading vortex indi-

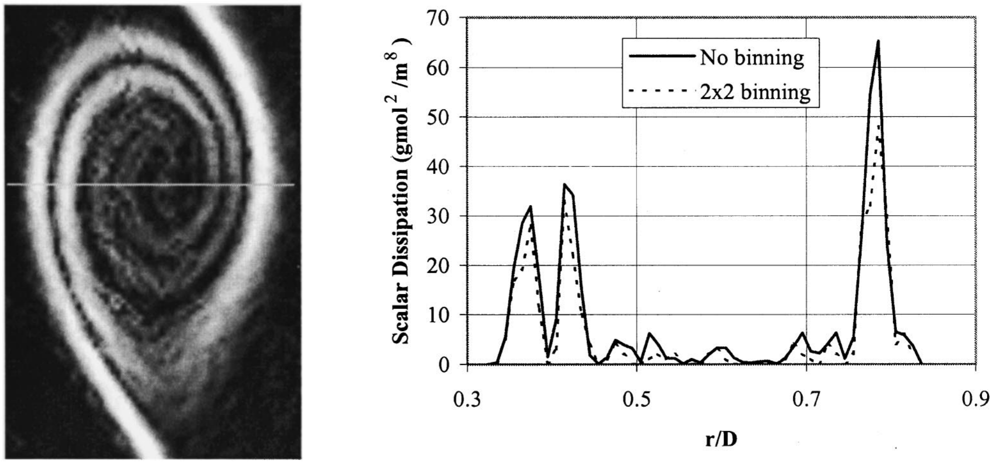

FIG. 15. Scalar dissipation layers of a vortex at 7.2 ms after the acoustic pulse. Gray-scale image is shown on a logarithmic scale due to an order of magnitude difference in scalar dissipation between the inner and outer layers.

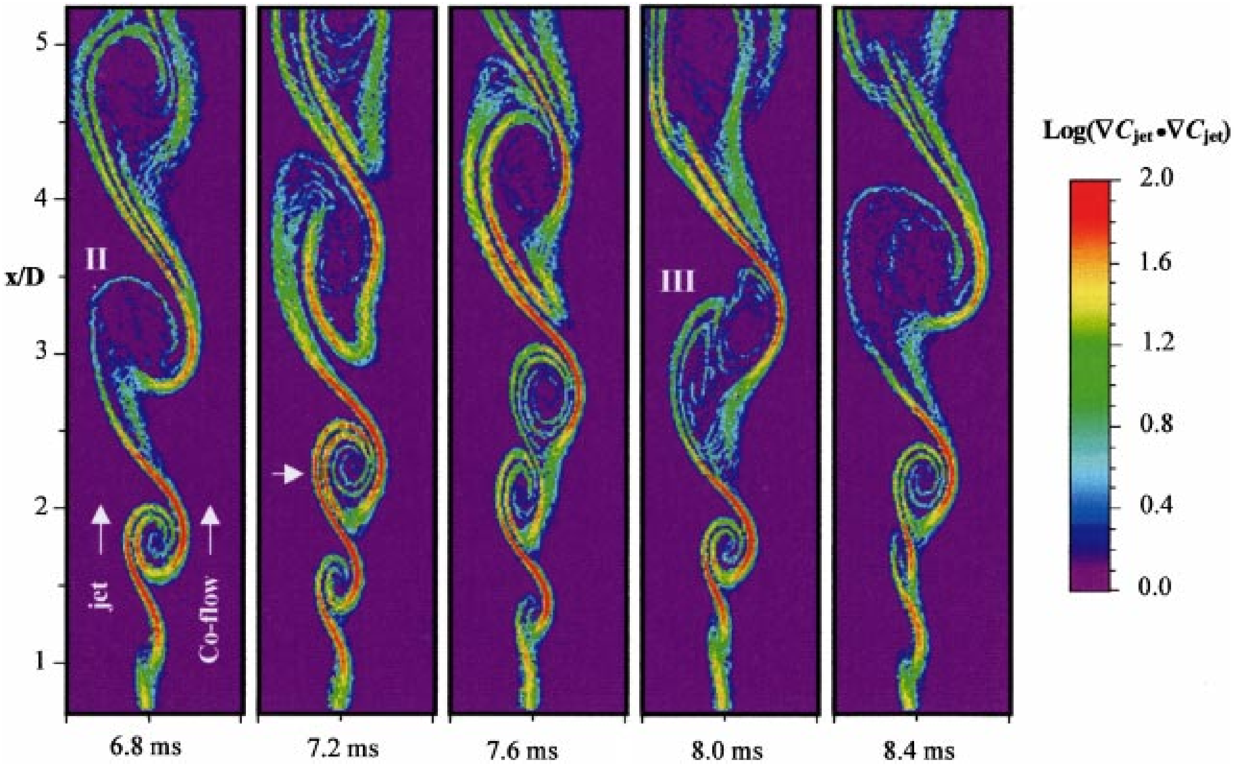

FIG. 16. Instantaneous, logarithmic maps of scalar dissipation, $\nabla C_{\mathrm{jet}} \cdot \nabla C_{\mathrm{jet}}$, from 6.8 to 8.4 ms after the acoustic pulse. The bottom scale is $0 < r/D < 1$, and the symbols II and III refer to different pairing events.

cates that co-flow fluid entrainment is being slowed by the approach of the trailing vortex. By 7.6 ms, the effects of the interaction are unmistakable. The orientation of the scalar dissipation layer at the bottom of the leading vortex indicates that co-flow fluid entrainment has ceased. For this reason, straining in the braid region decreases dramatically by 7.6 ms. A small break also appears in the bottom scalar dissipation layers of the trailing vortex at 7.6 ms, which confirms the reduced co-flow entrainment that was inferred earlier from slowed vortex growth. By 8.0 and 8.4 ms, almost no remnants of the initial vortices can be detected as vortex stretching and deformation increase the rate of homogenization.

The merged structure from pairing II is shown at 6.8 ms. Re-entrainment has clearly begun by this time, and the engulfment of co-flow fluid is clearly visible in the next image at 7.2 ms. A large-scale roll-up continues around the nearly homogeneous core at 7.6 and 8.0 ms, but the long tails of scalar dissipation indicate that most of the newly entrained jet fluid collects at the trailing end of the merged structure.

While these trends are in qualitative agreement with the vortex dynamics and stirredness calculations discussed earlier, more precise agreement on the timing of vortex mixing events can also be demonstrated. In Fig. 17, the magnitude of scalar dissipation is plotted as a function of time for the leading vortex of pairing III, measured in the jet side upper-braid region (see the arrow at 7.2 ms in Fig. 16). The scalar dissipation increases during the early stages of roll-up as pure co-flow fluid is entrained deeper into the vortex. The slope of the curve decreases steadily in this time period, perhaps due to the reduced spacing of layers during the roll-up process.[55] The magnitude of scalar dissipation then drops dramatically after 7.0 ms. This is also the time when a break in the bottom scalar dissipation layer of the leading vortex is first detected (see Fig. 16), and when the core region is first detected in Figs. 12 and 13. This indicates that accelerated scalar dissipation is occurring due to vortex interaction rather than the reduced spacing of layers described by Flohr and Vassilicos[55] in an isolated roll-up. As the vortices interact and begin to coalesce, the scalar dissipation falls asymptotically toward zero.

While the driven jet of the current investigation is not strictly a turbulent flow, the large-scale structures and sig-

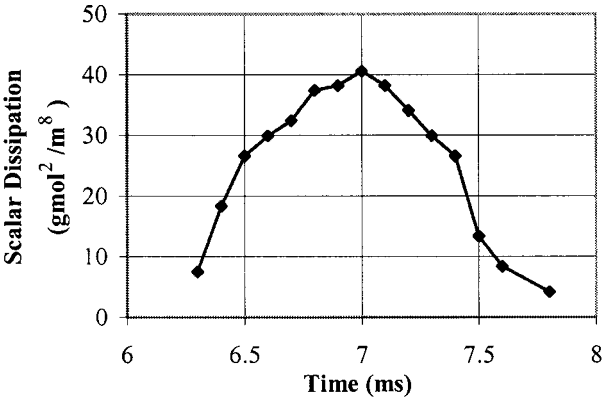

FIG. 17. Scalar dissipation in the jet side upper-braid region of the leading vortex of pairing III (see the arrow at 7.2 ms in Fig. 16).

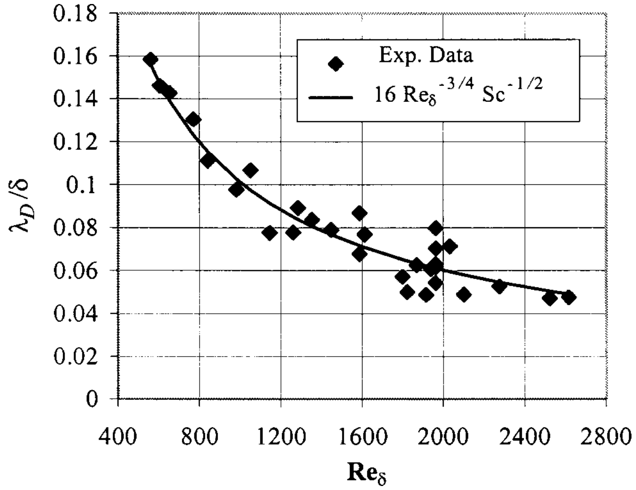

FIG. 18. Dependence of the diffusion length scale on the outer scale Reynolds number.

nificant vortex deformations result in nonlaminar characteristics. It is of interest, therefore, to determine if the scalar diffusion length scale in the pretransitional regime follows an inner-scale $\mathrm{Re}^{-3/4}$ or an outer-scale $\mathrm{Re}^{-1/2}$ dependence. Following the convention of Buch and Dahm,[31,32,57] Su and Clemens[33] measured the width of a scalar dissipation layer (λ_D) as the region that was within 20% of the local peak value. For the current investigation, the axial variation of the shear layer width, δ, was measured from an average of the entire time sequence of driven vortex images. The results for measurements taken only in the co-flow entrainment region (see arrow in Fig. 16) are shown in Fig. 18, and conform surprisingly well to a $\mathrm{Re}_\delta^{-3/4}$ inner-scale dependence.

VI. CONCLUSIONS

From the results of the current investigation, it is possible to identify several stages of vortex formation and merging in the near field of gaseous jets in terms of the mixing state and vortex dynamics. In order of occurrence, these are the vortex roll-up, interaction, coalescence, and re-entrainment stages. Vortex roll-up is distinguished by slightly increasing convection velocities, constant vortex growth rate, linearly increasing overall stirredness of the shear layer, the lack of a sizable core region, and a nonlinear increase in scalar dissipation.

The interaction phase begins as the trailing vortex approaches the leading vortex closely enough to interfere with the roll-up and co-flow entrainment process. This phase is characterized by the movement of the trailing vortex inward toward the jet core, movement of the leading vortex outward away from the jet core, and a sudden increase in vortex convection velocities. A dramatic increase in the size of the homogeneous core region of the leading vortex is also detected, and as a consequence of interrupting the entrainment process, the scalar dissipation in the leading vortex decreases dramatically. In previous work, the peak vorticity has been found to drop dramatically during this period.

The beginning of the pairing event coalescence results in a significant drop in the convection velocity of the leading vortex. The trailing vortex experiences gross deformation and stretching, and scalar dissipation in the core region decreases dramatically. The core diameter of the leading vortex continues to increase due to diffusion, but at a lower rate than in the interaction phase when co-flow entrainment is first interrupted. The homogenization process nears completion as the trailing vortex is deformed even further and is pulled into the core region of the leading vortex.

Re-entrainment is characterized by co-flow fluid engulfment, paired structure elongation, and possible additional interactions with other individual or paired vortices. The large incursion of co-flow fluid into the paired structure causes the typical ''kinked'' shape of these structures. Entrained jet fluid begins to surround the homogenized core, but most collects at the trailing end due to the lack of rotation.

The driven axisymmetric jet is a model flow that is useful for studying fundamental vortex behavior. The evolution of the mixing state during vortex formation and pairing accounts for trends that have been observed concerning vortex growth, trajectory, convection velocity, and vorticity. Although the flow structures in the near field of turbulent jets at high Reynolds numbers occur more randomly and in a more diverse fashion than in jets at lower Reynolds numbers, the mechanisms described in the current investigation capture the essential aspects of gaseous-jet, near-field vortex interactions.

ACKNOWLEDGMENTS

This work was supported by the National Science Foundation, Division of Chemical and Transport Systems, Grant No. CTS 94-23280, with Dr. R. E. A. Arndt and Dr. J. F. Foss as monitors. In addition, the authors would like to thank Gregory F. King for his helpful input on implementing the experimental and image processing procedures.

[1] S. C. Crow and F. H. Champagne, ''Orderly structure in jet turbulence,'' J. Fluid Mech. **48**, 547 (1971).
[2] C. D. Winant and F. K. Browand, ''Vortex pairing: The mechanism of turbulent mixing-layer growth at moderate Reynolds number,'' J. Fluid Mech. **63**, 237 (1974).
[3] W. J. A. Dahm and P. E. Dimotakis, ''Measurements of entrainment and mixing in turbulent jets,'' AIAA J. **25**, 1216 (1987).
[4] M. M. Koochesfahani and P. E. Dimotakis, ''Laser-Induced fluorescence measurements of mixed fluid concentration in a liquid plane shear layer,'' AIAA J. **23**, 1700 (1985).
[5] P. S. Karasso and M. G. Mungal, ''Scalar mixing and reaction in plane liquid shear layers,'' J. Fluid Mech. **323**, 23 (1997).
[6] N. T. Clemens and M. G. Mungal, ''Large-scale structure and entrainment in the supersonic mixing layer,'' J. Fluid Mech. **284**, 171 (1995).
[7] G. F. King, J. C. Dutton, and R. P. Lucht, ''Instantaneous, quantitative measurements of molecular mixing in the axisymmetric jet near field,'' Phys. Fluids **11**, 403 (1999).
[8] M. Winter, J. K. Lam, and M. B. Long, ''Techniques for high-speed digital imaging of gas concentrations in turbulent flows,'' Exp. Fluids **5**, 177 (1987).
[9] A. R. Ganji and R. F. Sawyer, ''Experimental study of the flowfield of a two-dimensional premixed turbulent flame,'' AIAA J. **18**, 817 (1980).
[10] B. M. Cetegen and N. Mohamad, ''Experiments on liquid mixing and reaction in a vortex,'' J. Fluid Mech. **249**, 391 (1993).
[11] K. B. Southerland, J. R. Porter III, W. J. A. Dahm, and K. A. Buch, ''An experimental study of the molecular mixing process in an axisymmetric laminar vortex ring,'' Phys. Fluids A **3**, 1385 (1991).
[12] J. E. Broadwell and M. G. Mungal, ''Molecular mixing and chemical reactions in turbulent shear layers,'' *22nd Symposium (International) on*

Combustion (The Combustion Institute, Pittsburgh, PA, 1988), p. 579.

[13] A. K. M. F. Hussain and K. B. M. Q. Zaman, ''Vortex pairing in a circular jet under controlled excitation. 2. Coherent structure dynamics,'' J. Fluid Mech. **101**, 493 (1980).

[14] F. R. Schauer, ''Thermal diffusion and flame structure in a laminar hydrogen jet diffusion flame,'' Ph.D. thesis, University of Illinois at Urbana–Champaign, 1998.

[15] F. F. Grinstein, E. J. Gutmark, T. P. Parr, D. M. Hanson-Parr, and U. Obeysekare, ''Streamwise and spanwise vortex interaction in an axisymmetric jet. A computational and experimental study,'' Phys. Fluids **8**, 1515 (1996).

[16] L. S. Huang and C. M. Ho, ''Small-scale transition in a plane mixing layer,'' J. Fluid Mech. **210**, 475 (1990).

[17] S. L. Wakelin and N. Riley, ''On the formation and propagation of vortex rings and pairs of rings,'' J. Fluid Mech. **332**, 121 (1997).

[18] J. S. Hewett and C. K. Medina, ''Flame-vortex interaction in a reacting vortex ring,'' Phys. Fluids **10**, 189 (1998).

[19] M. M. Rogers and R. D. Moser, ''Direct simulation of a self-similar turbulent mixing layer,'' Phys. Fluids **6**, 903 (1994).

[20] K. B. M. Q. Zaman and A. K. M. F. Hussain, ''Vortex pairing in a circular jet under controlled excitation. 1. General jet response,'' J. Fluid Mech. **101**, 449 (1980).

[21] R. L. Leboeuf and R. D. Mehta, ''Vortical structure morphology in the initial region of a forced mixing layer: Roll-up and pairing,'' J. Fluid Mech. **315**, 175 (1996).

[22] P. H. Paul, I. van Cruyningen, R. K. Hanson, and G. Kychakoff, ''High resolution digital flowfield imaging of jets,'' Exp. Fluids **9**, 241 (1990).

[23] R. D. Hancock, ''Laser diagnostic investigation of the structure of steady and driven hydrogen jet diffusion flames,'' Ph.D. thesis, University of Illinois at Urbana–Champaign, 1996.

[24] O. Inoue, ''Double-frequency forcing on spatially growing mixing layers,'' J. Fluid Mech. **234**, 553 (1992).

[25] R. A. Petersen and R. C. Clough, ''The influence of higher harmonics on vortex pairing in an axisymmetric mixing layer,'' J. Fluid Mech. **239**, 81 (1992).

[26] J. E. Broadwell and R. E. Breidenthal, ''A simple model of mixing and chemical reaction in a turbulent shear layer,'' J. Fluid Mech. **125**, 397 (1982).

[27] G. F. King, R. P. Lucht, and J. C. Dutton, ''Instantaneous dual-tracer PLIF measurements of molecular mixing in axisymmetric jets,'' AIAA Paper No. 97-0152, 35th AIAA Aerospace Sciences Meeting and Exhibit, Reno, NV, 1997.

[28] A. N. Kolmogorov, ''The local structure of turbulence in incompressible viscous fluid for very large Reynolds numbers,'' Dokl. Akad. Nauk SSSR **30**, 301 (1941).

[29] A. N. Kolmogorov, ''Dissipation of energy in locally isotropic turbulence,'' Dokl. Akad. Nauk SSSR **32**, 16 (1941).

[30] G. K. Batchelor, *The Theory of Homogeneous Turbulence* (Cambridge University Press, Cambridge, 1953).

[31] K. A. Buch and W. J. A. Dahm, ''Experimental study of the fine-scale structure of conserved scalar mixing in turbulent shear flows. 1. $\mathrm{Sc}\gg 1$,'' J. Fluid Mech. **317**, 21 (1996).

[32] K. A. Buch and W. J. A. Dahm, ''Experimental study of the fine-scale structure of conserved scalar mixing in turbulent shear flows. 2. $\mathrm{Sc}\sim 1$,'' J. Fluid Mech. **364**, 1 (1998).

[33] L. K. Su and N. T. Clemens, ''The Structure of the Three-Dimensional Scalar Gradient in Gas-Phase Planar Turbulent Jets,'' AIAA Paper No. 98-0429, 36th AIAA Aerospace Sciences Meeting and Exhibit, Reno, NV, 1998.

[34] D. R. Dowling and P. E. Dimotakis, ''Similarity of the concentration field of gas-phase turbulent jets,'' J. Fluid Mech. **218**, 109 (1990).

[35] R. Verzicco and P. Orlandi, ''Mixedness in the formation of a vortex ring,'' Phys. Fluids **7**, 1513 (1995).

[36] R. P. Lucht, ''Applications of laser-induced fluorescence spectroscopy for combustion and plasma diagnostics,'' in *Laser Spectroscopy and its Applications*, edited by L. J. Radzemski, R. W. Solarz, and J. Paisner (Marcel Dekker, New York, 1987).

[37] A. C. Eckbreth, *Laser Diagnostics for Combustion Temperature and Species*, 1st ed. (Abacus Press, Cambridge, MA, 1988).

[38] P. E. Dimotakis, R. C. Miake-Lye, and D. A. Papantoniou, ''Structure and dynamics of round turbulent jets,'' Phys. Fluids **26**, 3185 (1983).

[39] D. Papantoniou and E. J. List, ''Large-scale structure in the far field of buoyant jets,'' J. Fluid Mech. **209**, 151 (1989).

[40] W. J. A. Dahm and P. E. Dimotakis, ''Mixing at large Schmidt number in the self-similar far field of turbulent jets,'' J. Fluid Mech. **217**, 299 (1990).

[41] A. Lozano, B. Yip, and R. K. Hanson, ''Acetone: A tracer for concentration measurements in gaseous flows by planar laser-induced fluorescence,'' Exp. Fluids **13**, 369 (1992).

[42] B. Yip, M. F. Miller, A. Lozano, and R. K. Hanson, ''A combined OH/acetone planar laser-induced fluorescence imaging technique for visualizing combusting flows,'' Exp. Fluids **17**, 330 (1994).

[43] N. T. Clemens and P. H. Paul, ''Effects of heat release on the near field flow structure of hydrogen jet diffusion flames,'' Combust. Flame **102**, 271 (1995).

[44] M. F. Miller, T. C. Island, J. M. Seitzman, C. T. Bowman, M. G. Mungal, and R. K. Hanson, ''An experimental investigation of supersonic reacting mixing layers,'' AIAA Paper No. 94-0823, 32nd AIAA Aerospace Sciences Meeting and Exhibit, Reno, NV, 1994.

[45] J. M. Seitzman, M. F. Miller, B. K. McMillin, R. K. Hanson, P. A. DeBarber, and C. F. Hess, ''Multiple scalar planar fluorescence imaging for reacting flows,'' AIAA Paper No. 94-0228, 32nd AIAA Aerospace Sciences Meeting and Exhibit, Reno, NV, 1994.

[46] M. M. Koochesfahani, P. E. Dimotakis, and J. E. Broadwell, ''A 'flip' experiment in a chemically reacting turbulent mixing layer,'' AIAA J. **23**, 1191 (1985).

[47] B. Yip, A. Lozano, and R. K. Hanson, ''Sensitized phosphorescence: a gas phase molecular mixing diagnostic,'' Exp. Fluids **17**, 16 (1994).

[48] N. T. Clemens and P. H. Paul, ''Scalar measurements in compressible axisymmetric mixing layers,'' Phys. Fluids **7**, 1071 (1995).

[49] T. C. Island, W. D. Urban, and M. G. Mungal, ''Quantitative scalar measurements in compressible mixing layers,'' AIAA Paper No. 96-0685, 34th AIAA Aerospace Sciences Meeting and Exhibit, Reno, NV, 1996.

[50] G. F. King, R. P. Lucht, and J. C. Dutton, ''Quantitative dual-tracer planar laser-induced fluorescence measurements of molecular mixing,'' Opt. Lett. **22**, 633 (1997).

[51] A. Lozano, ''Laser-excited luminescent tracers for planar concentration measurements in gaseous jets,'' Stanford University, HTGL Report No. T-284, 1992.

[52] P. H. Paul, J. A. Gray, J. L. Durant, and J. W. Thoman, ''Collisional quenching corrections for laser-induced fluorescence measurements of NO $A\,^2\Sigma^+$,'' AIAA J. **32**, 1670 (1994).

[53] R. D. Hancock, F. R. Schauer, R. P. Lucht, V. R. Katta, and K. Y. Hsu, ''Thermal diffusion effects and vortex-flame interactions in hydrogen jet diffusion flames,'' *26th Symposium (International) on Combustion* (The Combustion Institute, Pittsburgh, PA, 1996), p. 1087.

[54] C. M. Ho and L. S. Huang, ''Subharmonics and vortex merging in mixing layers,'' J. Fluid Mech. **119**, 443 (1982).

[55] P. Flohr and J. C. Vassilicos, ''Accelerated scalar dissipation in a vortex,'' J. Fluid Mech. **348**, 295 (1997).

[56] W. J. A. Dahm, L. K. Su, and K. M. Tacina, ''Four-dimensional measurements of vector fields in turbulent flows,'' AIAA Paper No. 96-1987, 27th AIAA Fluid Dynamics Conference, New Orleans, LA, 1996.

[57] K. A. Buch and W. J. A. Dahm, ''Fine scale structure of conserved scalar mixing in turbulent flows: $\mathrm{Sc}\gg 1$, $\mathrm{Sc}=1$, and implications for reacting flows,'' University of Michigan, Report No. 026779-5, 1991.